Transverse coherence of photon pairs generated in spontaneous parametric down-conversion

Martin Hamar, Jan Peřina Jr., Ondřej Haderka, and Václav Michálek
Joint Laboratory of Optics of Palacký University and Institute of Physics of Academy of Sciences of the Czech Republic, 17. listopadu 50a, CZ-77207 Olomouc, Czech Republic
(Received 26 January 2010; published 21 April 2010)

Coherence properties of the down-converted beams generated in spontaneous parametric down-conversion are investigated in detail using an iCCD camera. Experimental results are compared with those from a theoretical model developed for pulsed pumping with a Gaussian transverse profile. The results allow us to tailor the shape of correlation area of the signal and idler photons using pump-field and crystal parameters. As an example, splitting of a correlation area caused by a two-peak pump-field spectrum is experimentally studied.

DOI: 10.1103/PhysRevA.81.043827 PACS number(s): 42.65.Lm, 42.50.Ar

I. INTRODUCTION

Light emitted from spontaneous parametric down-conversion in a nonlinear crystal is composed of photon pairs. Two photons comprising a photon pair are called a signal and an idler photon for historic reasons. The first theoretical investigation of this process has been done in year 1968 [1]. Already this study has revealed that frequencies and emission directions of two photons in a pair are fully determined by the laws of energy and momentum conservations. For this reason, there occurs a strong correlation (entanglement) between properties of the signal and idler photons. In an ideal case of infinitely long and wide nonlinear crystal and monochromatic plane-wave pumping, a plane-wave signal photon at frequency ω_s belongs just to one plane-wave idler photon at frequency ω_i that is determined by the conservation of energy. Emission angles of these photons are given by the momentum conservation that forms phase-matching conditions. Possible signal (and similarly idler) emission directions lie on a cone which axis coincides with the pump-beam direction of propagation.

However, real experimental conditions have enforced the consideration of crystals with finite dimensions [2,3], pump beams with nonzero divergence [4,5], as well as pulsed pumping [6–9]. During this investigation, the approximation based on a multidimensional Gaussian spectral two-photon amplitude has been found extraordinarily useful [10,11]. The developed models have revealed that spatial characteristics of a pump beam are transferred to certain extent to these of a photon pair generated in a nonlinear crystal, especially in case of short crystals [12–15]. These models have also been useful in quantifying real effects in applied experimental setups utilizing photon pairs [16,17]. They have also been recently extended to photonic [18,19] and wave-guiding [20–25] structures. Also effects at nonlinear boundaries have been taken into account [26,27].

In this article, we continue the previous investigations of spatial photon-pair properties [28–31] by experimental study of transverse profiles of the down-converted beams as well as correlation areas of the signal and idler photons using an iCCD camera [32–34]. Special attention is paid to the role of pump-beam parameters. Experimental results are compared with a theoretical model that considers Gaussian spectrum and elliptical pump-beam profile. We note that also sensitive CCD cameras have been found useful in investigations of spatial properties of more intense twin beams [35–37].

The article is organized as follows. A theoretical model is presented in Sec. II. Section III brings theoretical analysis of parameters of a correlation area as well as spectral properties of the down-converted fields. An experimental method based on the use of an iCCD camera is discussed in detail in Sec. IV. The experimentally observed dependence of parameters of the correlation area on pump-beam characteristics and crystal length is reported in Sec. V. Sec. VI is devoted to splitting of the correlation area and its experimental observation. Conclusions are drawn in Sec. VII.

II. THEORY

The process of spontaneous parametric down-conversion is described by the following interaction Hamiltonian $\hat{H}_{\rm int}$ [2,16,38]:

$$\hat{H}_{\rm int}(t) = \varepsilon_0 \int_V d\mathbf{r}\chi^{(2)} : \mathbf{E}_p^{(+)}(\mathbf{r},t)\hat{\mathbf{E}}_s^{(-)}(\mathbf{r},t)\hat{\mathbf{E}}_i^{(-)}(\mathbf{r},t) + \text{H.c.}, \tag{1}$$

where $\mathbf{E}_p^{(+)}$ is the positive-frequency part of the pump electric-field amplitude, whereas $\hat{\mathbf{E}}_s^{(-)}$ ($\hat{\mathbf{E}}_i^{(-)}$) stands for the negative-frequency part of the signal (idler) electric-field amplitude operator. Symbol $\chi^{(2)}$ means the second-order susceptibility tensor and : is shorthand for tensor reduction with respect to its three indices. Susceptibility of vacuum is denoted as ε_0, interaction volume as V and H.c. substitutes the Hermitian-conjugated term.

We further consider parametric down-conversion in a $LiIO_3$ crystal with an optical axis perpendicular to the z axis of fields' propagation direction and type-I interaction. The pump field is assumed to be polarized vertically (it propagates as an extraordinary wave), whereas the signal and idler fields are polarized horizontally (they propagate as ordinary waves). In this specific configuration, scalar optical fields are sufficient for the description. The interacting optical fields can then be decomposed into monochromatic plane waves with frequencies ω_a and wave vectors $\mathbf{k}_a$:

$$\hat{E}_a^{(+)}(\mathbf{r},t) = \int d\mathbf{k}_a \hat{E}_a^{(+)}(\mathbf{k}_a)\exp(i\mathbf{k}_a\mathbf{r} - i\omega_a t) + \text{H.c.}; \quad a = p,s,i. \tag{2}$$

The signal and idler fields at a single-photon level have to be described quantally and so their spectral amplitudes $\hat{E}_a^{(+)}(\mathbf{k}_a)$

can be expressed as $\hat{E}_a^{(+)}(\mathbf{k}_a) = i\sqrt{\hbar\omega_a}/\sqrt{2\varepsilon_0 c\mathcal{A}n_a(\omega_a)}\hat{a}_a(\mathbf{k}_a)$ using annihilation operators $\hat{a}_a(\mathbf{k}_a)$ that remove one photon from a plane-wave mode $\mathbf{k}_a$ in field a. Symbol $\hbar$ stands for the reduced Planck constant, c is speed of light in vacuum, $\mathcal{A}$ transverse area of a beam, and n_a means index of refraction in field a.

Under these conditions, the interaction Hamiltonian $\hat{H}_{\mathrm{int}}$ in Eq. (1) takes the form [10]:

$$\begin{aligned}\hat{H}_{\mathrm{int}}(t) = A_n\left(\omega_s^0,\omega_i^0\right)&\int d\mathbf{k}_s \int d\mathbf{k}_i \int d\mathbf{k}_p E_p^{(+)}(\mathbf{k}_p)\\ &\times \exp\{i[\omega(\mathbf{k}_p)-\omega(\mathbf{k}_s)-\omega(\mathbf{k}_i)]t\}\\ &\times \int_V d\mathbf{r}\exp[-i(\mathbf{k}_p-\mathbf{k}_s-\mathbf{k}_i)\mathbf{r}]\\ &\times \hat{a}_s^\dagger(\mathbf{k}_s)\hat{a}_i^\dagger(\mathbf{k}_i)+\mathrm{H.c.}\end{aligned} \tag{3}$$

We have assumed in deriving Eq. (3) that the function $A_n(\omega_s,\omega_i) = -\hbar\sqrt{\omega_s\omega_i}\chi^{(2)}/(2c\mathcal{A}\sqrt{n_s(\omega_s)n_i(\omega_i)})$ is a slowly varying function of frequencies ω_s and ω_i and can be approximated by its value taken at the central frequencies ω_s^0 and ω_i^0.

A quantum state $|\Psi\rangle$ of a generated photon pair can be obtained after solving the Schrödinger equation up to the first power of the interaction constant that results in the formula:

$$|\Psi\rangle = -\frac{i}{\hbar}\int_{-\infty}^{\infty} dt\,\hat{H}_{\mathrm{int}}(t)|\mathrm{vac}\rangle; \tag{4}$$

where $|\mathrm{vac}\rangle$ means the vacuum state. Substitution of the interaction Hamiltonian $\hat{H}_{\mathrm{int}}$ from Eq. (3) into Eq. (4) provides the following form for the quantum state $|\Psi\rangle$ [4,16,39–41]:

$$|\Psi\rangle = \int d\mathbf{k}_s \int d\mathbf{k}_i\, S(\mathbf{k}_s,\mathbf{k}_i)\hat{a}_s^\dagger(\mathbf{k}_s)\hat{a}_i^\dagger(\mathbf{k}_i)|\mathrm{vac}\rangle, \tag{5}$$

where the newly introduced two-photon amplitude S takes the form:

$$\begin{aligned}S(\mathbf{k}_s,\mathbf{k}_i) = A_n'&\int d\mathbf{k}_p E_p^{(+)}(\mathbf{k}_p)\delta(\omega_p-\omega_s-\omega_i)\\ &\times\int_V d\mathbf{r}\exp[-i(\mathbf{k}_p-\mathbf{k}_s-\mathbf{k}_i)\mathbf{r}]\end{aligned} \tag{6}$$

and $A_n' = -2\pi i/\hbar A_n(\omega_s^0,\omega_i^0)$. We note that squared modulus $|S(\mathbf{k}_s,\mathbf{k}_i)|^2$ of the two-photon amplitude gives us the probability density of simultaneous generation of a signal photon with wave vector $\mathbf{k}_s$ and its twin with wave vector $\mathbf{k}_i$.

Spectral resolution is usually not found in experiments with photon pairs and then the photon-pair coincidence-count rate is linearly proportional to the fourth-order correlation function $G_{s,i}$ defined as:

$$\begin{aligned}&G_{s,i}(\xi_s,\delta_s,\xi_i,\delta_i)\\ &= \frac{\sin(\xi_s)\sin(\xi_i)}{c^6}\int d\omega_s\omega_s^2\\ &\quad\times\int d\omega_i\omega_i^2|h(\omega_s)h(\omega_i)|^2|S(\xi_s,\delta_s,\omega_s,\xi_i,\delta_i,\omega_i)|^2;\end{aligned} \tag{7}$$

$S(\xi_s,\delta_s,\omega_s,\xi_i,\delta_i,\omega_i)\equiv S(\mathbf{k}_s,\mathbf{k}_i)$. The propagation direction of a photon is parameterized by radial emission angles ξ_a (determining declination from the z axis) and azimuthal emission angles δ_a (describing rotation around the z axis starting from the x axis); $a = s,i$ (see also Fig. 8 later). Functions h_s and h_i introduced in Eq. (7) describe amplitude spectral and/or geometrical filtering of photons in front of detectors.

More detailed information is contained in intensity spectrum S_s of a signal field assuming photon pairs emitted into the fixed signal- and idler-photon directions given by angles ξ_s, δ_s, ξ_i, and δ_i:

$$\begin{aligned}&S_s(\omega_s;\xi_s,\delta_s,\xi_i,\delta_i)\\ &= \frac{\sin(\xi_s)\sin(\xi_i)\omega_s^2|h(\omega_s)|^2}{c^6}\\ &\quad\times\int d\omega_i\omega_i^2|h(\omega_i)|^2|S(\xi_s,\delta_s,\omega_s,\xi_i,\delta_i,\omega_i)|^2.\end{aligned} \tag{8}$$

If the signal-photon emission direction described by angles ξ_s and δ_s is not resolved, an integrated signal-field emission spectrum S_s^{int} is observed:

$$S_s^{\mathrm{int}}(\omega_s;\xi_i,\delta_i) = \int_{-\pi/2}^{\pi/2} d\xi_s\int_{-\pi}^{\pi} d\delta_s\, S_s(\omega_s;\xi_s,\delta_s,\xi_i,\delta_i). \tag{9}$$

Similar formulas as given in Eqs. (8) and (9) can be derived also for the idler field.

On the other hand, excluding resolution in emission directions, spectral correlations between the signal and idler fields are characterized by a two-photon spectral amplitude $\Phi_{s,i}$ which squared modulus is defined as:

$$\begin{aligned}|\Phi_{s,i}(\omega_s,\omega_i)|^2 = \frac{\omega_s^2\omega_i^2}{c^6}&\int d\delta_s\int d\xi_s\int d\delta_i\int d\xi_i\sin(\xi_s)\\ &\times\sin(\xi_i)|h(\omega_s)h(\omega_i)|^2|S(\xi_s,\delta_s,\omega_s,\xi_i,\delta_i,\omega_i)|^2.\end{aligned} \tag{10}$$

We further consider a Gaussian pump beam with the electric-field amplitude $E_p^{(+)}$ in the from:

$$\begin{aligned}E_p^{(+)}(\mathbf{r},t) = \int d\omega_p A_p(\omega_p)&\exp(i\mathbf{k}_{pz}z - i\omega_p t)\\ &\times\frac{1}{W_{px}(z)}\exp\left[-\frac{x^2}{W_{px}^2(z)}\right]\exp\left[-ik_p\frac{x^2}{2R_{px}^2(z)}\right]\\ &\times\frac{1}{W_{py}(z)}\exp\left[-\frac{y^2}{W_{py}^2(z)}\right]\exp\left[-ik_p\frac{y^2}{2R_{py}^2(z)}\right]\\ &\times\exp[i\zeta_p(z)];\end{aligned} \tag{11}$$

$k_p = |\mathbf{k}_p|$. The functions W_{pa}, R_{pa}, and ζ_p are defined as:

$$W_{pa}(z) = W_{pa}^0\sqrt{1+\frac{z^2}{\left(z_{pa}^0\right)^2}},\quad W_{pa}^0 = \sqrt{\frac{2z_{pa}^0}{k_p}}, \tag{12}$$

$$R_{pa}(z) = z\left[1+\frac{(z_{pa}^0)^2}{z^2}\right],\quad a = x,y, \tag{13}$$

$$\zeta_p(z) = \left[\arctan\left(z/z_{px}^0\right)+\arctan\left(z/z_{py}^0\right)\right]/2. \tag{14}$$

The function A_p introduced in Eq. (11) gives the pump-field amplitude temporal spectrum. Constants z_{px}^0 and z_{py}^0 describe positions of waists with radii W_{px}^0 and W_{py}^0 in the x and y directions, respectively. Function $W_{px}(z)$ [$W_{py}(z)$] gives a radius of the beam in the x [y] direction and with wavefront curvature $R_{px}(z)$ [$R_{py}(z)$] at position z.

We assume that the nonlinear crystal is sufficiently short so that changes of the pump-field amplitude $E_p^{(+)}$ in the transverse plane along the z axis can be neglected. In this case, the pump-field amplitude $E_p^{(+)}$ can be characterized both by its temporal spectrum $A_p(\omega_p)$ and spatial spectrum $F_p(k_{px},k_{py})$ in the transverse plane:

$$E_p^{(+)}(\mathbf{r},t) = \int d\omega_p A_p(\omega_p) \int d\mathbf{k}_{px} \int d\mathbf{k}_{py} F_p(\mathbf{k}_{px},\mathbf{k}_{py}) \times \exp(i\mathbf{k}_{px}x)\exp(i\mathbf{k}_{py}y)\exp(i\mathbf{k}_{pz}z)\exp(-i\omega_p t). \tag{15}$$

The spatial spectrum F_p corresponding to the Gaussian beam written in Eq. (11) and propagating along the z axis can be expressed as:

$$F_p(\mathbf{k}_{px},\mathbf{k}_{py}) = \frac{1}{W_{px}(z_0)W_{py}(z_0)} \frac{2}{\bar{W}_{px}\bar{W}_{py}} \times \exp\left[-\frac{\mathbf{k}_{px}^2}{\bar{W}_{px}^2}\right]\exp\left[-\frac{\mathbf{k}_{py}^2}{\bar{W}_{py}^2}\right]\exp[i\zeta_p(z_0)], \tag{16}$$

where the position z_0 lies inside the crystal. Complex spectral half-widths $\bar{W}_{px}$ and $\bar{W}_{py}$ of the spatial spectrum in the transverse plane are given as follows:

$$\bar{W}_{pa} = 2\sqrt{\frac{1}{W_{pa}^2(z_0)} + \frac{ik_p}{2R_{pa}^2(z_0)}}, \qquad a = x,y. \tag{17}$$

In the following we consider a Gaussian chirped pump pulse which temporal amplitude spectrum A_p can be expressed in the form:

$$A_p(\omega_p) = \xi_p \frac{\tau_p}{\sqrt{2(1+ia_p)}} \exp\left[-\frac{\tau_p^2}{4(1+ia_p)}\omega_p^2\right]. \tag{18}$$

In Eq. (18), τ_p denotes pump-pulse duration, a_p stands for a chirp parameter, and ξ_p is the pump-field amplitude. We note that the amplitude width $\Delta\omega_p$ (given as full width at $1/e$ of the maximum) of the pulse written in Eq. (18) equals $4\sqrt{(1+a_p^2)}/\tau_p$.

Considering the pump-field amplitude $E_p^{(+)}$ as given in Eq. (15) the two-photon amplitude S defined in Eq. (6) can be recast into the form:

$$\begin{aligned} &S(\xi_s,\delta_s,\omega_s,\xi_i,\delta_i,\omega_i) \\ &\quad = cA_p(\omega_s+\omega_i)F_p(\mathbf{k}_{sx}+\mathbf{k}_{ix},\mathbf{k}_{sy}+\mathbf{k}_{iy}) \\ &\qquad \times L_z \mathrm{sinc}\left\{\frac{[\mathbf{k}_{pz}(\omega_s+\omega_i)-\mathbf{k}_{sz}(\omega_s)-\mathbf{k}_{iz}(\omega_i)]L_z}{2}\right\} \\ &\qquad \times \exp\left\{-i\frac{[\mathbf{k}_{pz}(\omega_s+\omega_i)-\mathbf{k}_{sz}(\omega_s)-\mathbf{k}_{iz}(\omega_i)]L_z}{2}\right\}; \end{aligned} \tag{19}$$

$\mathrm{sinc}(x) = \sin(x)/x$. In deriving Eq. (19), we have assumed that the crystal extents from $z = -L_z$ to $z = 0$, L_z being the crystal length. The transverse profile of crystal is also assumed to be sufficiently wide.

III. CORRELATION AREA, SPECTRAL PROPERTIES

Correlation area is defined by the profile of probability density of detecting a signal photon in the direction described by angles (ξ_s,δ_s) provided that its idler twin has been detected in a fixed direction given by angles (ξ_i,δ_i). In coherence theory, this probability is given by the fourth-order correlation function $G_{s,i}$ defined in Eq. (7). Because the correlation function $G_{s,i}$ is usually a smooth function of its arguments, it can be conveniently parameterized using angular widths (given as full-widths at $1/e$ of maximum) in the radial $(\Delta\xi_s)$ and azimuthal $(\Delta\delta_s)$ directions. In general, parameters of the correlation area depend on properties of crystal material as well as crystal length, pump-field spectral bandwidth, and transverse pump-beam profile. The last two parameters allow us to tailor characteristics of the correlation area in wide ranges.

In the theoretical analysis of Sec. III, we use radial (ξ) and azimuthal (δ) angles inside a nonlinear crystal. The reason is that we want to exclude the effect of mixing in spatial and frequency domains at the output plane of the crystal in the discussion. However, starting from Sec. IV radial (ξ) and azimuthal (δ) angles outside the nonlinear crystal are naturally used in the presentation of experimental results.

In radial direction, crystal length and pump-field spectral bandwidth as well as transverse pump-beam profile play a role. The dependence of radial width of the correlation area on the crystal length L_z emerges through the phase-matching condition in the z direction. This condition is mathematically described by the expression $\mathrm{sinc}(\Delta\mathbf{k}_z L_z/2)$ in Eq. (19); $\Delta\mathbf{k}_z = \mathbf{k}_{pz} - \mathbf{k}_{sz} - \mathbf{k}_{iz}$. Actual radial width is determined by this condition and conservation of energy $(\omega_p = \omega_s + \omega_i)$. According to the formula in Eq. (17), the longer the crystal, the smaller the radial width. Analytical theory also predicts narrowing of the signal- and idler-field spectra with an increasing crystal length. If pulsed pumping is considered, the wider the pump-field spectrum, the greater the radial width and also the greater the signal-field spectral width [compare Figs. 1(c) and 1(d) with Figs. 1(a) and 1(b). This can be understood as follows: more pump-field frequencies are present in a wider pump-field spectrum and so more signal- and idler-field frequencies are allowed to obey the phase-matching conditions in the z direction and conservation of energy. In more detail and following the graphs in Figs. 1(c) and 1(d), signal-field photons with different wavelengths are emitted into different radial emission angles ξ_s. Superposition of photon fields emitted into different radial emission angles ξ_s then broadens the overall signal-field spectrum. It is important to note that all idler-field photons have nearly the same wavelengths, which means that signal-field photons emitted into different radial emission angles ξ_s use different wavelengths of the pulsed-pump spectrum. The transverse pump-beam profile affects the radial width through the phase-matching condition in the radial plane. This radial phase-matching condition is an additional requirement that must be fulfilled by a generated photon pair. Qualitatively, the more the pump beam is focused, the wider its spatial spectrum in radial direction and so the weaker the radial phase-matching condition. However, this dependence is quite small in radial angles, as follows from the comparison of graphs in Figs. 1(a) and 1(b) with Figs. 1(e) and 1(f). On the other hand, focusing of the pump beam leads

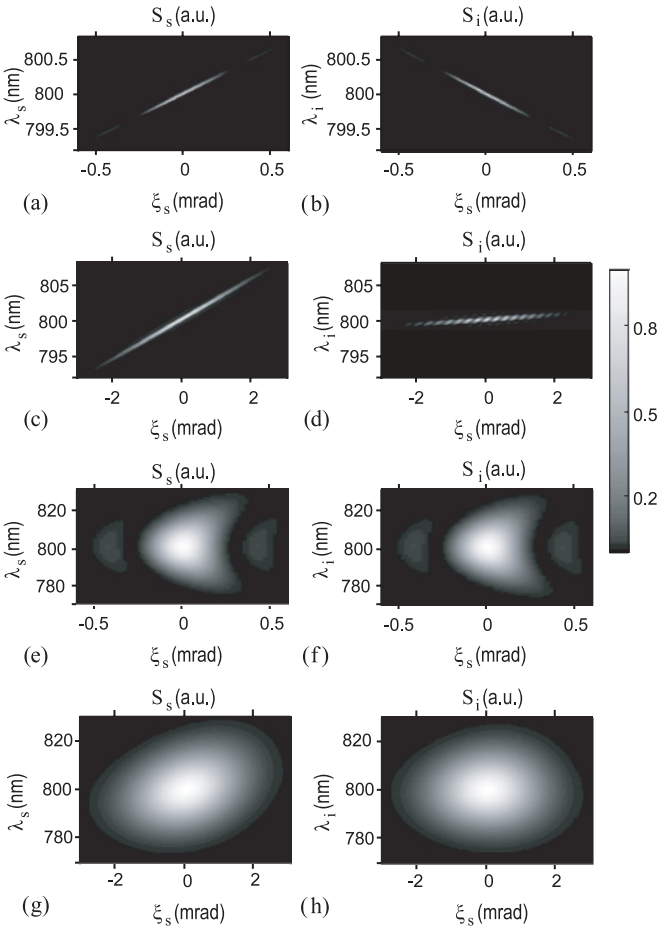

FIG. 1. Contour plots of signal- $[S_s(\lambda_s)]$ and idler-field $[S_i(\lambda_i)]$ intensity spectra as they depend on radial signal-field emission angle ξ_s; idler-field emission angle ξ_i is fixed. Spectra are determined for cw plane-wave pumping (a and b), pulsed plane-wave pumping (c and d; $\Delta\lambda_p = 2.8$ nm), cw focused pumping (e and f; $W_p^{0,f} = 20$ μm) and pulsed focused pumping (g and h, $\Delta\lambda_p = 2.8$ nm, $W_p^{0,f} = W_{px}^{0,f} = W_{py}^{0,f} = 20$ μm) for $L_z = 5$ mm.

to considerable broadening of the signal- and idler-field spectra in all radial emission directions. Finally, if a focused pulsed pump beam is assumed [see Figs. 1(g) and 1(h)], broadening of the correlation area in radial direction as well as broadening of the overall signal- and idler-field spectra is observed due to a final pump-field spectral width. On the top, broadening of the signal- and idler-field spectra corresponding to any radial emission angle ξ_s occurs as a consequence of pump-beam focusing. This behavior is related to the fact that indexes of refraction of the interacting fields are nearly constant inside the correlation area. We can say, in general, that spectral widths of the signal and idler fields behave qualitatively in the same way as the radial width of correlation area.

Comparison of the signal- and idler-field spectra in Figs. 1(c) and 1(d) valid for pulsed pumping with those in Figs. 1(a) and 1(b) for cw pumping leads to a remarkable observation. Photon pairs generated into different signal-photon radial emission angles ξ_s use different pump-field frequencies. There occurs spectral asymmetry between the signal and idler fields that originates in different detection

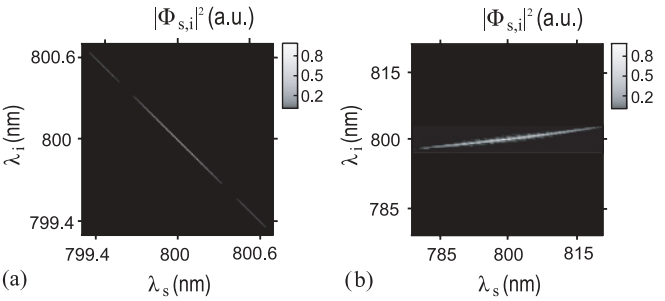

FIG. 2. Contour plots of squared modulus $|\Phi_{s,i}|^2$ of two-photon spectral amplitude for (a) cw and (b) pulsed ($\Delta\lambda_p = 8.5$ nm) plane-wave pumping; $L_z = 5$ mm.

angles considered; whereas the idler-field detection angle is fixed, the angle of a signal-photon detection varies. This asymmetry determines the preferred direction of the signal- and idler-field frequency correlations as they are visible in the shape of squared modulus $|\Phi_{s,i}|^2$ of two-photon spectral amplitude introduced in Eq. (10) [a large signal-field detector is assumed]. Contour plot of the squared modulus $|\Phi_{s,i}|^2$ of two-photon amplitude has a typical cigar shape. In the cw case, the main axis of this cigar is rotated 45° counterclockwise with respect to the λ_i axis [see Fig. 2(a)] in order to describe perfect frequency anticorrelation. If pulsed pumping is taken into account, the cigar axis tends to rotates clockwise; the broader the pump-field spectrum, the greater the rotation angle. Even states with positively correlated signal- and idler-field frequencies can be observed for sufficiently broad pump-field spectra [see Fig. 2(b)]. We note that different dispersion properties at different propagation angles have been fully exploited in the method of achromatic phase matching that allows us to generate photon pairs with an arbitrary orientation of the two-photon spectral amplitude [15,42,43].

The azimuthal width of correlation area is determined predominantly by a pump-beam transverse profile for geometric reasons. To be more specific, it is the pump-beam spatial spectrum in azimuthal direction that affects the azimuthal extension of the correlation area through the phase-matching conditions in the azimuthal direction. As material dispersion characteristics of the crystal are rotationally symmetric with respect to the z axis (signal and idler fields propagate as ordinary waves), the azimuthal width of spatial pump-beam spectrum does not practically influence spectral properties of the signal and idler fields.

We illustrate the dependence of correlation area on pump-beam focusing using a 5-mm-long crystal and both cw and pulsed pumping in Fig. 3. We can see in Fig. 3(a) that the signal-field azimuthal width $\Delta\delta_s$ is inversely proportional to the width $W_p^{0,f}$ (full width at $1/e$ of the maximum; $W_p^{0,f} \equiv W_{px}^{0,f} = W_{py}^{0,f}$) of the pump-beam waist whereas the radial width $\Delta\xi_s$ does not practically depend on the width $W_p^{0,f}$ of the pump-beam waist. This is caused by the fact that the phase-matching condition in the z direction is much stronger than that in radial direction for a 5-mm-long crystal and so the radial width $\Delta\xi_s$ is sensitive only to the pump-field spectral width in this case. Pulsed pumping gives a broader correlation area in radial direction as well as broader signal-field spectrum compared to cw case [see Fig. 3(b)]. Increasing pump-beam

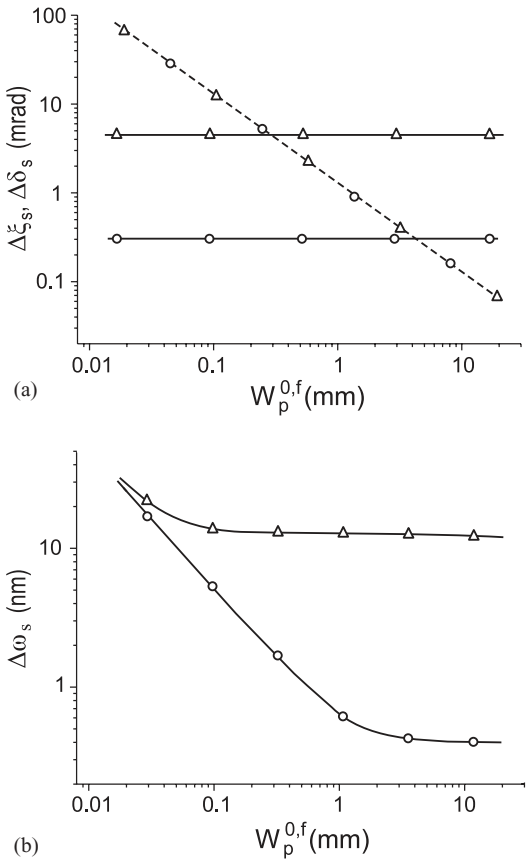

FIG. 3. (a) Radial ($\Delta\xi_s$, solid curves) and azimuthal ($\Delta\delta_s$, dashed curves) widths of correlation area and (b) signal-field spectral width $\Delta\omega_s$ as they depend on width $W_p^{0,f}$ of the pump-beam waist for pulsed ($\Delta\lambda_p = 5$ nm, triangles) and cw ($\Delta\lambda_p = 0.03$ nm, circles) pumping; $L_z = 5$ mm. Logarithmic scales on the x and y axes are used.

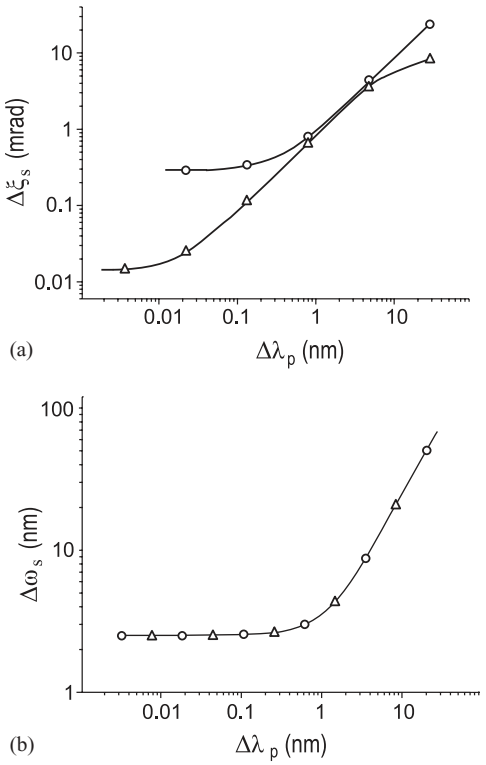

FIG. 4. (a) Radial width $\Delta\xi_s$ of correlation area and (b) signal-field spectral width $\Delta\omega_s$ as functions of pump-field spectral width $\Delta\lambda_p$ for a 5-mm-long (circles) and 10-cm-long (triangles) crystal assuming a focused pump beam; $W_p^{0,f} = 200$ μm. Logarithmic scales on the x and y axes are used.

focusing releases phase-matching conditions and naturally leads to a broader signal-field spectrum.

Contrary to the azimuthal width, the radial width $\Delta\xi_s$ depends on the pump-field spectral width $\Delta\lambda_p$. The larger the pump-field spectral width $\Delta\lambda_p$ the greater the radial width $\Delta\xi_s$ and also the greater the signal-field spectral width $\Delta\omega_s$, as documented in Fig. 4 for a focused pump beam. We can also see in Fig. 4(a) that the radial width $\Delta\xi_s$ reaches a constant value for sufficiently narrow pump-field spectra. This value is determined by the phase-matching condition in the z direction for the central pump-field frequency ω_p^0 and so depends on the crystal length L_z (together with material dispersion properties of the crystal). The longer the crystal the smaller the radial width $\Delta\xi_s$.

The above described dependencies allow to generate photon pairs with highly elliptic profiles of the correlation area provided that the pump-beam profile in the transverse plane is highly elliptic. As an example, we consider a pump beam having $W_{py}^{0,f}/W_{px}^{0,f} = 10$. The dependence of the radial ($\Delta\xi_s$) and azimuthal ($\Delta\delta_s$) widths and signal-field spectral width $\Delta\omega_s$ on the central azimuthal signal-photon emission angle δ_{s0} is shown in Fig. 5 in this case. Whereas the radial and azimuthal widths are comparable for the azimuthal signal-field emission angle $\delta_{s0} = \pi/2$, their ratio $\Delta\delta_s/\Delta\xi_s$ equals approx. 20 for $\delta_{s0} = 0$. Focusing the pump beam from 200 to 20 μm in radial direction results in doubling the signal-field spectral width $\Delta\omega_s$ as documented in Fig. 5(b) [see also Figs. 1(a) and 1(e)].

IV. EXPERIMENTAL SETUP

We have used a negative uniaxial crystal made of $LiIO_3$ cut for noncritical phase matching, i.e., the optical axis was perpendicular to the pump-beam propagation direction. We have considered crystals of two different lengths ($L_z = 2$ mm and 5 mm) pumped both by cw and pulsed lasers. As for cw pumping, a semiconductor laser Cube 405 (Coherent) delivered 31.6 mW at 405 nm and with spectral bandwidth $\Delta\lambda_p = 1.7$ nm. The second-harmonic field of an amplified femtosecond Ti:sapphire system (Mira+RegA, Coherent) providing pulses at 800 nm and ~250 fs long was used in the pulsed regime. The mean SHG power was 2.5 mW at the crystal input for a repetition rate of 11 kHz. Spectral bandwidth was adjusted between 4.8 and 7.4 nm by fine tuning of the SHG process. A dispersion prism was used to separate the fundamental and SHG beams (for details, see Fig. 6).

Transverse profile of the pump beam and its divergence were controlled by changing the focal length of converging lens L1 or using a beam expander (BE2X, Thorlabs). The used focal lengths f_{L1} of lens L1 laid in the interval from 30 to 75 cm. As we wanted the pump beam to be as homogeneous as possible along the z axis, we chose the distance z_{L1} between the lens L1 and the nonlinear crystal such that the beam waist was

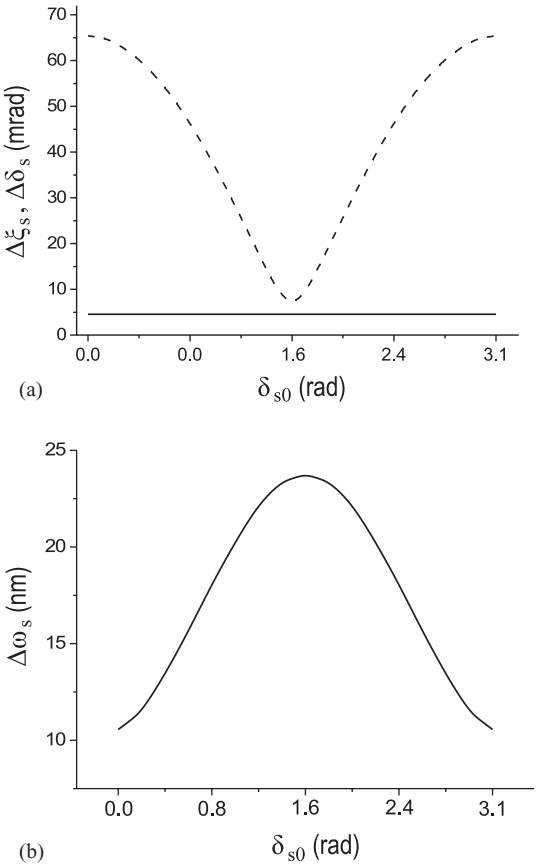

FIG. 5. (a) Radial ($\Delta\xi_s$, solid curve) and azimuthal ($\Delta\delta_s$, dashed curve) widths of correlation area and (b) signal-field spectral width $\Delta\omega_s$ as they depend on central azimuthal signal-field emission angle δ_{s0} for a highly elliptic pulsed pump beam ($W_{px}^{0,f} = 200\ \mu$m, $W_{py}^{0,f} = 20\ \mu$m, $\Delta\lambda_p = 5$ nm); $L_z = 5$ mm.

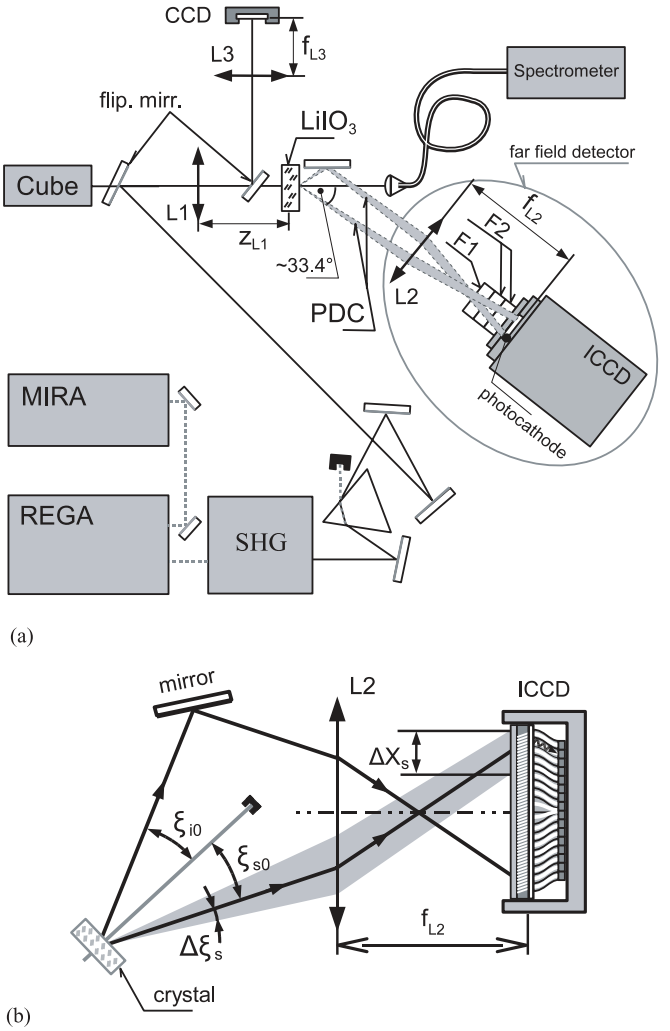

FIG. 6. Experimental setup used for the determination of angular widths. (a) Entire setup that includes both cw and pulsed pumping as well as pump-beam diagnostics (for more details, see the text). (b) Detail of the setup showing paths of the signal and idler beams.

placed far behind the crystal, i.e., $z_{L1} < f_{L1}$. Spatial spectrum of the pump beam in the transverse plane as a very important parameter in our experiment was measured by a CCD camera (Lu085M, Lumenera) placed at the focal plane of a converging lens L3. Spatial spectra in horizontal and vertical directions were determined as marginal spectra and parameters $\tilde{W}_{px}$ and $\tilde{W}_{py}$ characterizing their widths were found after fitting the experimental data. A fiber-optic spectrometer (HR4000CG-UV-NIR, Ocean Optics) was used to obtain the pump-beam temporal spectrum after propagation through the nonlinear crystal.

The experiment was done with photon pairs degenerate in frequencies ($\lambda_{s0} = \lambda_{i0} = 800$ nm) and emitted in opposite parts of a cone layer (the central radial emission angle was 33.4° behind the crystal). As shown in Fig. 6(b) the signal beam was captured directly by a detector, whereas the idler beam propagated to the detector after being reflected on a high-reflectivity mirror. Both beams were detected on a photocathode of an iCCD camera with image intensifier (PI-MAX:512-HQ, Princeton Instruments). Before detection, both beams were transformed using a converging lens L2, one narrow-bandwidth filter, and two high-pass edge filters. The geometry of the setup was chosen such that the lens L2 mapped the signal and idler photon emission angles to positions at the photocathode; the photocathode was placed in the focal plane of lens L2. For convenience, lenses L2 with different focal lengths ($f_{L2} = 12.5$, 15, and 25 cm) were used. The applied bandwidth filter was 11 nm wide and centered at 800 nm. Edge filters (Andover, ANDV7862) had high transmittances at 800 nm (98%) and blocked wavelengths below 666 nm.

An active area of the photocathode in the form of a rectangle, 12.36 mm wide (see Fig. 7), was divided into 512×512 pixels. Spatial resolution of the camera was 38 μm (FWHM) and its main limitation came from imperfect contrast transfer in the image intensifier. In order to make data acquisition faster the resolution was further decreased by grouping 4×4 or 8×8 pixels into one superpixel in the hardware of the camera. Consequently, several tens of camera frames were captured in 1 s. The overall quantum detection efficiency including components between the crystal and photocathode was 7%, as derived from covariance of the signal and idler photon numbers. Widths of the signal and idler strips are given by the bandwidth filter and lens L2 focal length. As for timing, a 10-ns-long gate of the camera was used synchronously with laser pulses. In the cw case, a 2-μs-long gate was applied together with internal triggering. This timing together with appropriate pump-field intensities assured that

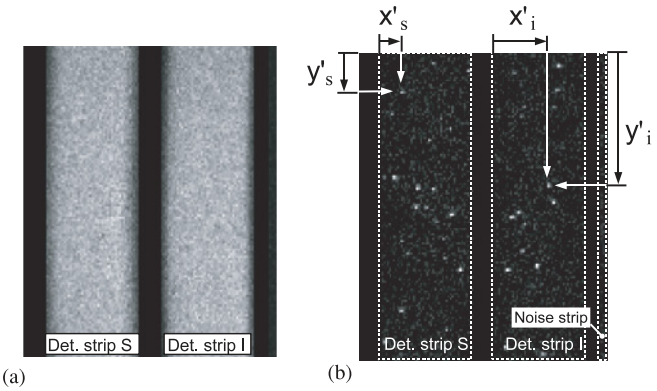

FIG. 7. Photocathode with registered photons after (a) illumination by light coming from 20 000 consecutive pump pulses and (b) one pump pulse. The signal and idler strips image small sections of the cone layer and are slightly curved. The curvatures are oriented in the same sense in both strips because the idler beam is reflected on a mirror.

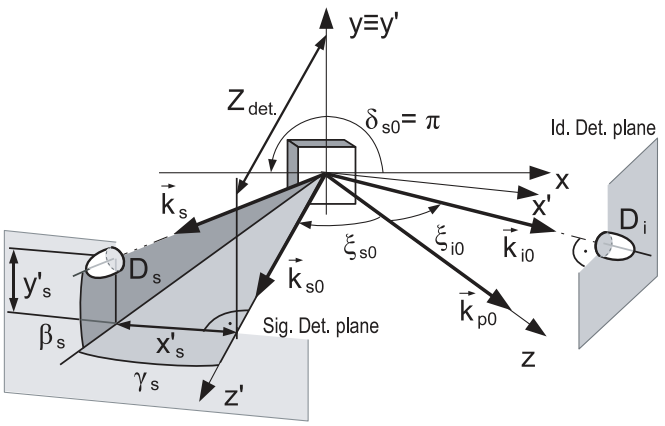

FIG. 8. Sketch showing the geometry of signal and idler beams. The photon emission direction is described by radial (ξ) and azimuthal (δ) emission angles. In detector plane, Cartesian coordinates x' and y' are useful. Photons propagation directions are then conveniently parameterized by angles β and γ.

the probability of detecting two photons in a single superpixel was negligible. In other words, the number of detection events divided by quantum detection efficiency had to be much lower than the number of superpixels.

The level of noise was monitored in the third narrow strip; 1.82% of detection events came from noise. Detailed analysis has shown that 90% of noise photons were red photons originating from fluorescence inside the crystal. Scattered pump photons contributed by 8.4% and only 1.6% of noise counts were dark counts of the iCCD camera.

The experimental signal-idler correlation functions g_x and g_y in the transverse plane described by horizontal (x') and vertical (y') coordinates of the reference system in this plane have been determined after processing many experimental frames. The formula for the determination of correlation function g_x can be written as follows [see also Fig. 7(b)]:

$$g_x(x'_s,x'_i) = \sum_{p=1}^{N}\sum_{m=1}^{M_p}\sum_{l=1}^{L_p}\delta\left(x'^{pm}_s - x'_s\right)\delta\left(x'^{pl}_i - x'_i\right). \quad (20)$$

In Eq. (20), p indexes frames (N gives the number of frames) and m (l) counts signal (idler) detection events [up to M_p (L_p) in the p-th frame]. Symbol x'^{pl}_s (x'^{pl}_i) denotes horizontal position of the l-th detection in the signal (idler) strip of the p-th frame. Correlations in the vertical direction given by the correlation function g_y can be determined similarly. The formula in Eq. (20) takes into account all possible combinations of pairwise detection events. Only some of them correspond to detection of both photons from one pair. The remaining combinations are artificial in the sense that they do not correspond to detection of a photon pair. This poses the following restriction to the method. The number of artificial combinations that occur at random positions has to be large enough in order to create a plateau in a 2D graph of correlation function $g_x(x'_s,x'_i)$. Real detections of photon pairs are then visible on the top of this plateau (see Fig. 9 later).

Cartesian coordinates x'_j and y'_j, $j = s,i$, in the transverse plane can be conveniently transformed into angles β_j and γ_j measured from the middle (x'^{cent}_j, y'^{cent}_j) of the j-th strip and defined in Fig. 8 using the formulas:

$$\begin{aligned}\gamma_j &= \arctan\left[\left(x'_j - x'^{\text{cent}}_j\right)/f_{L2}\right],\\ \beta_j &= \arctan\left[\left(y'_j - y'^{\text{cent}}_j\right)/f_{L2}\cos(\gamma_j)\right], \quad j = s,i;\end{aligned} \quad (21)$$

f_{L2} means the focal length of lens L2. Angles β_j and γ_j are related to radial and azimuthal angles ξ_j and δ_j by the following transformation:

$$\begin{aligned}\beta_j &= \arcsin[\sin(\xi_j)\sin(\delta_j)],\\ \gamma_j &= \arctan[\tan(\xi_j)\cos(\delta_j)] - \xi_{j,\text{det}}, \quad j = s,i,\end{aligned} \quad (22)$$

where the radial angle $\xi_{j,\text{det}}$ describes the position of a detector in beam j.

V. EXPERIMENTAL DETERMINATION OF PARAMETERS OF CORRELATION AREA

In the experiment, spatial and temporal spectra of the pump beam have been characterized first. Typical results are shown in Figs. 9(a) and 9(b) and have been used in the model for the determination of expected parameters of the correlation area. The correlation area, or more specifically its radial and angular profiles, have been characterized using histograms $g_x(x'_s,x'_i)$ and $g_y(y'_s,y'_i)$. Histogram $g_x(x'_s,x'_i)$ [$g_y(y'_s,y'_i)$] gives the number of paired detections with a signal photon detected at position x'_s [y'_s] together with an idler photon registered at position x'_i [y'_i]. These histograms usually contain experimental data from several hundreds of thousands of frames. As graphs in Figs. 9(c) and 9(d) show detections of correlated photon pairs lead to higher values in histograms g_x and g_y around diagonals going from upper-left to lower-right corners of the plots. Finite spreads of these diagonals have their origin in nonperfect phase matching and can be characterized by their widths $\Delta x'_s$ and $\Delta y'_s$. Or more conveniently by uncertainties in the determination of angles β_s and γ_s; $\Delta\beta_s \approx \Delta y'_s/f_{L2}$ and $\Delta\gamma_s \approx \Delta x'_s/f_{L2}$. As detailed inspection of the histogram g_x (g_y) in Fig. 9(c) [Fig. 9(d)] has shown, cuts of this histogram along the lines with constant values of x'_i (y'_i) do

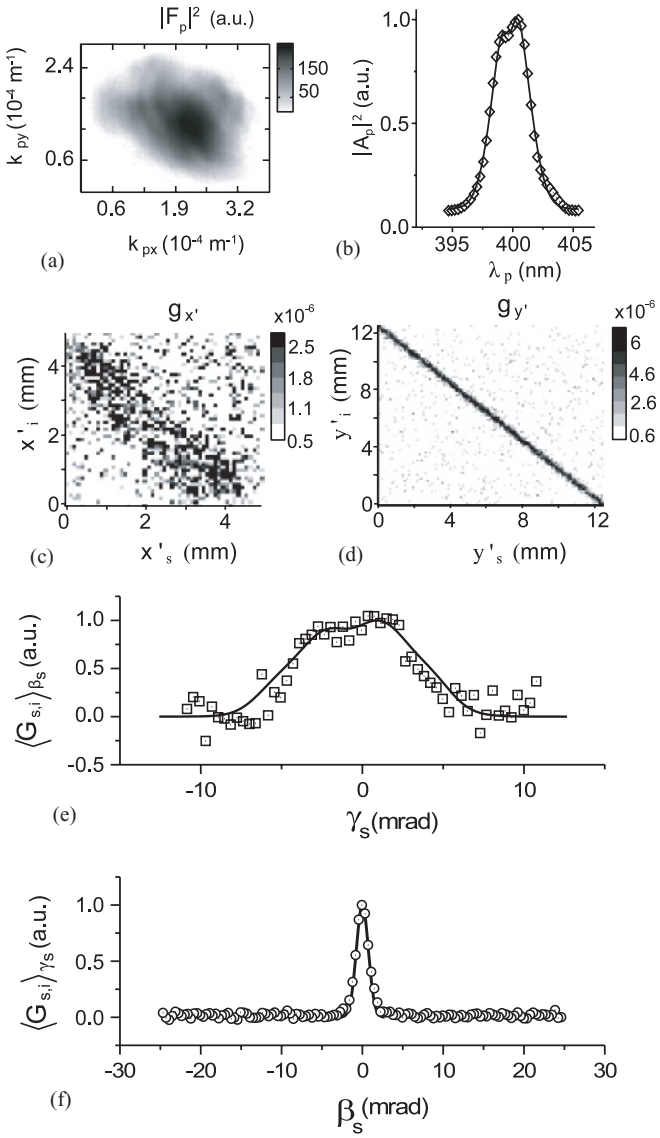

FIG. 9. Typical measurement of a correlation area for pulsed pumping having 327 600 frames; $L_z = 5$ mm. (a) Spatial spectrum of the pump beam determined in the focal plane of lens L3. (b) Temporal intensity spectrum of the pump beam as determined by a spectrometer (diamonds), solid line represents a multipeak Gaussian fit. Experimental histograms (c) $g_x(x_s',x_i')$ and (d) $g_y(y_s',y_i')$. Experimental (e) radial $\langle G_{s,i}\rangle_{\beta_s}$ and (f) azimuthal $\langle G_{s,i}\rangle_{\gamma_s}$ cross sections of the correlation area (rectangles, circles) together with theoretical predictions (solid lines).

not depend on the value of x_i' (y_i'). This reflects the fact that idler photons detected at different positions inside the investigated area on the photocathode have identical (signal-photon) correlation areas. This allows us to combine the data obtained for idler photons detected at different positions together and increase the measurement precision this way. This approach thus provides the radial cross section $\langle G_{s,i}\rangle_{\beta_s}$ of the correlation area along the radial angle γ_s as a mean value over all possible values of the signal-field azimuthal angle β_s. Moreover, consideration of different idler-photon detection positions means averaging over the angles γ_i and β_i. The averaging is indicated by symbol $\langle\rangle$. Mathematically, the radial cross section $\langle G_{s,i}\rangle_{\beta_s}$ expressed in the coordinate x_s' can be derived along the formula

$$\langle G_{s,i}\rangle_{\beta_s}(x_s') = \sum_{x_i'} g\left[x_s' - x_s'^{\mathrm{mid}}(x_i'), x_i'\right], \tag{23}$$

where the function $x_s'^{\mathrm{mid}}(x_i')$ gives the central position (given as a locus) of the cut of the histogram $g(x_s',x_i')$ for a fixed value of the coordinate x_i'. In the theory, the radial cross section $\langle G_{s,i}\rangle_{\beta_s}$ is determined using the fourth-order correlation function $G_{s,i}$ written in Eq. (7), substitution of angles ξ_s, δ_s, ξ_i, and δ_i by angles γ_s, β_s, γ_i, and β_i [inverse transformation to that in Eq. (22)], and, finally, integration over the angles β_s, γ_i, and β_i. Similarly, the azimuthal cross section $\langle G_{s,i}\rangle_{\gamma_s}$ of the correlation area along the azimuthal angle β_s arises after averaging over the angles γ_s, γ_i, and β_i and can be determined by a formula analogous to that given in Eq. (21). The radial and azimuthal cross sections $\langle G_{s,i}\rangle_{\beta_s}$ and $\langle G_{s,i}\rangle_{\gamma_s}$ corresponding to the pump beam with characteristics defined in Figs. 9(a) and 9(b) are plotted in Figs. 9(e) and 9(f). Solid lines in Figs. 9(e) and 9(f) refer to the results of numerical model and are in a good agreement with the experimental data.

The radial width $\langle\Delta\gamma_s\rangle_{\beta_s}$ (measured as full width at $1/e$ of the maximum) of radial cross section $\langle G_{s,i}\rangle_{\beta_s}$ depends mainly on the pump-beam spectral width $\Delta\lambda_p$. It holds that the greater the pump-beam width $\Delta\lambda_p$ the larger the radial width $\langle\Delta\gamma_s\rangle_{\beta_s}$, as documented in Fig. 10 for crystals 2 and 5 mm long. In the experiment, 11-nm-wide frequency filters have been applied to cut noise. However, certain amount of photons comprising a photon pair has also been blocked. According to the theoretical model, this has also resulted in a small narrowing of the radial cut of the correlation area (compare solid and dashed curves in Fig. 10). The theoretical curve in Fig. 10 has been experimentally confirmed for several values of the width $W_{px}^{0,f}$ of pump-beam waist both for cw and pulsed pumping.

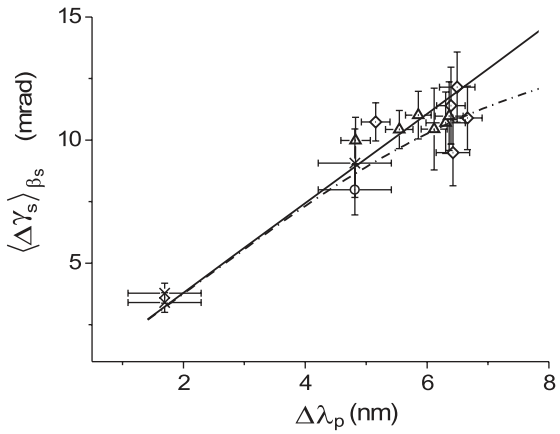

FIG. 10. Radial width $\langle\Delta\gamma_s\rangle_{\beta_s}$ as a function of pump-beam spectral width $\Delta\lambda_p$. Experimental points have been obtained for $L_z = 5$ mm, $W_{px}^{0,f} > 140$ μm (triangles), $L_z = 5$ mm, $W_{px}^{0,f} < 140$ μm (diamonds), $L_z = 2$ mm, $W_{px}^{0,f} > 140$ μm (crosses), and $L_z = 2$ mm, $W_{px}^{0,f} < 140$ μm (circles) both for cw and pulsed pumping. The theoretical model gives the same dependence for both crystal lengths L_z in cases without (solid curve) as well as with (dashed curve, 11-nm wide) spectral filters.

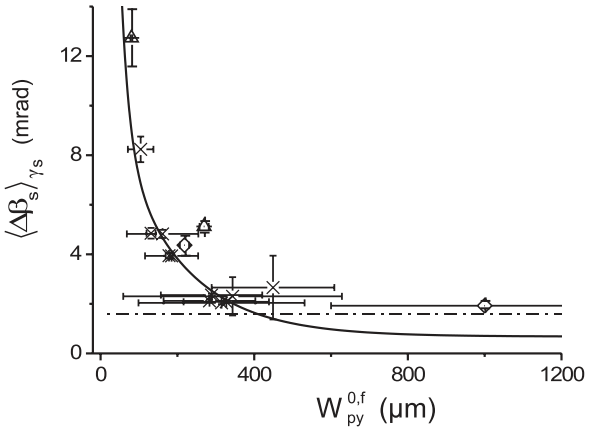

FIG. 11. Angular width $\langle \Delta\beta_s \rangle_{\gamma_s}$ as it depends on width $W_{py}^{0,f}$ of the pump-beam waist for pulsed (crosses and triangles) and cw (diamonds) pumping. Two-mm-long (triangles and diamonds) and 5-mm-long (crosses) crystals were used in experiment. The theoretical model predicts the same dependence for both crystals (solid curve). The dashed horizontal line indicates the resolution limit given by the camera superpixel size.

On the other hand, and in our geometry, it is the width $W_{py}^{0,f}$ of the pump-beam waist that determines the angular width $\langle \Delta\beta_s \rangle_{\gamma_s}$ of angular cross section $\langle G_{s,i} \rangle_{\gamma_s}$. Predictions of the model for 2- and 5-mm-long crystals are shown in Fig. 11 by a solid curve. This curve has been checked experimentally for several values of the width $W_{py}^{0,f}$ of the pump-beam waist both for cw and pulsed pumping. We note that these curves do not depend on the pump-beam spectral width $\Delta\lambda_p$. We can see in Fig. 11 that the measured points agree with the theoretical curve for smaller values of the width $W_{py}^{0,f}$. Larger values of the width $W_{py}^{0,f}$ lead to small angular widths $\langle \Delta\beta_s \rangle_{\gamma_s}$ that could not be correctly measured because of the limited spatial resolution of the iCCD camera.

VI. ENGINEERING THE SHAPE OF A CORRELATION AREA

As the above results have shown parameters of a correlation area can be efficiently controlled using pump-beam parameters, namely temporal spectrum and transverse profile. Even the shape of correlation area can be considerably modified. Splitting of the correlation area into two parts that occurs as a consequence of splitting of the pump-field temporal spectrum can serve as an example. Using our femtosecond pump system, we were able to experimentally confirm this behavior. We have generated a pump beam with the spatial spectrum given in Fig. 12(a). Its temporal spectrum containing two peaks, as was acquired by a spectrometer, is plotted in Fig. 12(b). The experimental radial width $\langle \Delta\gamma_s \rangle_{\beta_s}$ of cross section $\langle G_{s,i} \rangle_{\beta_s}$ given in Fig. 12(c) shows that the two-peak structure of the pump-field spectrum resulted in splitting of the correlation area into two parts. On the other hand, and in agreement with the theory, the angular cross section $\langle G_{s,i} \rangle_{\gamma_s}$ was not affected by the pump-field spectral splitting [see Fig. 12(d)]. For comparison, the theoretical profile of the correlation area given by the correlation function $G_{s,i}$ and appropriate for the pump-beam parameters given in Figs. 12(a) and 12(b)

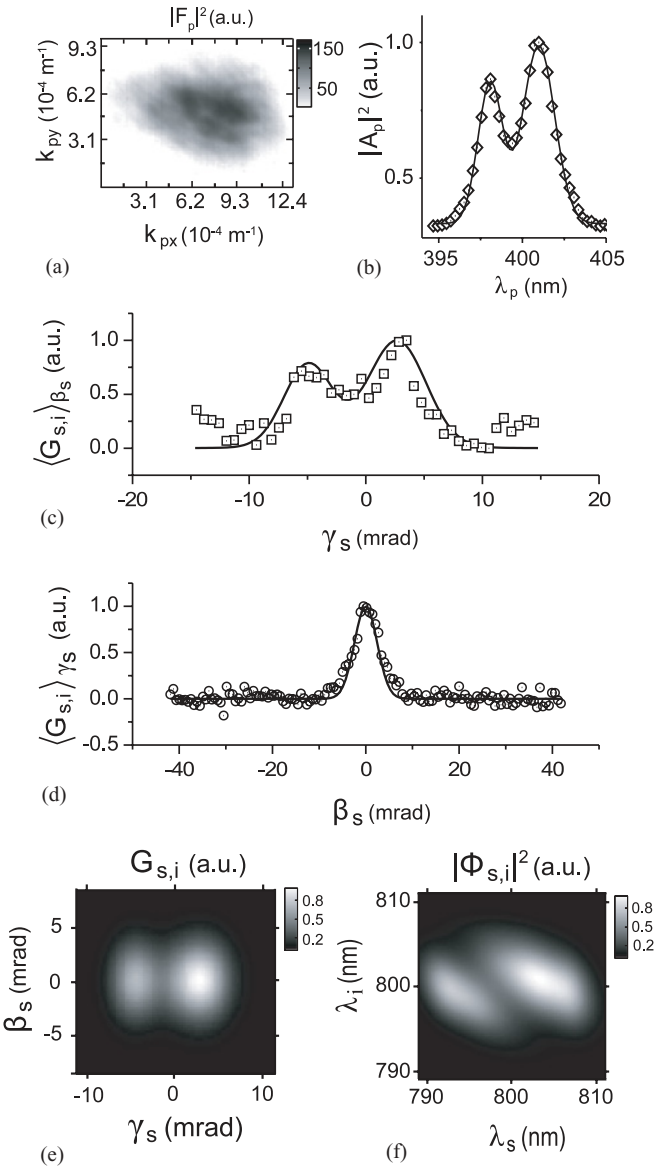

FIG. 12. Determination of a correlation area for pulsed pumping composed of two spectral peaks; $L_z = 5$ mm. (a) Spatial spectrum of the pump beam. (b) Temporal pump-field intensity spectrum (experimental points are indicated by diamonds, solid line represents a multipeak Gaussian fit). Experimental (c) radial $\langle G_{s,i} \rangle_{\beta_s}$ and (d) azimuthal $\langle G_{s,i} \rangle_{\gamma_s}$ cross sections of the correlation area (rectangles and circles) together with theoretical predictions (solid line). (e) Contour plot of the theoretical correlation function $G_{s,i}$. (f) Contour plot of the squared modulus $|\Phi_{s,i}|^2$ of the theoretical two-photon spectral amplitude.

is plotted in Fig. 12(e). It indicates a good agreement of the model with experimental data. Moreover, the squared modulus $|\Phi_{s,i}|^2$ of theoretical two-photon spectral amplitude reveals that splitting of the correlation area is accompanied by splitting of the signal-field spectrum [see Fig. 12(f)].

VII. CONCLUSIONS

We have developed a method for the determination of profiles of a correlation area using an intensified CCD camera.

Single detection events in many experimental frames are processed and provide histograms from which cross-sections of the correlation area can be recovered. This method has been used for investigations of the dependence of parameters of the correlation area on pump-beam characteristics and crystal length. The experimentally obtained curves have been successfully compared with a theoretical model giving fourth-order correlation functions. Radial profile of the correlation area depends mainly on pump-field spectrum and crystal length. On the other hand, azimuthal profile of the correlation area is sensitive only to the transverse profile of the pump beam. Splitting of the correlation area caused by a two-peak structure of the pump-field spectrum has also been experimentally observed.

ACKNOWLEDGMENTS

This research has been supported by the projects IAA100100713 of GA AV ČR, 1M06002, and COST OC 09026 of the Ministry of Education of the Czech Republic.

[1] T. G. Giallorenziho and C. L. Tang, Phys. Rev. **166**, 225 (1968).
[2] C. K. Hong and L. Mandel, Phys. Rev. A **31**, 2409 (1985).
[3] L. J. Wang, X. Y. Zou, and L. Mandel, Phys. Rev. A **44**, 4614 (1991).
[4] T. P. Grayson and G. A. Barbosa, Phys. Rev. A **49**, 2948 (1994).
[5] O. Steuernagel and H. Rabitz, Opt. Commun. **154**, 285 (1998).
[6] T. E. Keller and M. H. Rubin, Phys. Rev. A **56**, 1534 (1997).
[7] G. Di Giuseppe, L. Haiberger, F. De Martini, and A. V. Sergienko, Phys. Rev. A **56**, R21 (1997).
[8] W. P. Grice and I. A. Walmsley, Phys. Rev. A **56**, 1627 (1997).
[9] J. Perina Jr., A. V. Sergienko, B. M. Jost, B. E. A. Saleh, and M. C. Teich, Phys. Rev. A **59**, 2359 (1999).
[10] A. Joobeur, B. E. A. Saleh, and M. C. Teich, Phys. Rev. A **50**, 3349 (1994).
[11] A. Joobeur, B. E. A. Saleh, T. S. Larchuk, and M. C. Teich, Phys. Rev. A **53**, 4360 (1996).
[12] M. B. Nasr, A. F. Abouraddy, M. C. Booth, B. E. A. Saleh, A. V. Sergienko, M. C. Teich, M. Kempe, and R. Wolleschensky, Phys. Rev. A **65**, 023816 (2002).
[13] C. H. Monken, P. H. Souto Ribeiro, and S. Padua, Phys. Rev. A **57**, 3123 (1998).
[14] S. P. Walborn, A. N. de Oliveira, R. S. Thebaldi, and C. H. Monken, Phys. Rev. A **69**, 023811 (2004).
[15] G. Molina-Terriza, S. Minardi, Y. Deyanova, C. I. Osorio, M. Hendrych, and J. P. Torres, Phys. Rev. A **72**, 065802 (2005).
[16] Y. Shih, Rep. Prog. Phys. **66**, 1009 (2003).
[17] C. K. Law and J. H. Eberly, Phys. Rev. Lett. **92**, 127903 (2004).
[18] M. Centini, J. Perina Jr., L. Sciscione, C. Sibilia, M. Scalora, M. J. Bloemer, and M. Bertolotti, Phys. Rev. A **72**, 033806 (2005).
[19] J. Perina Jr., M. Centini, C. Sibilia, M. Bertolotti, and M. Scalora, Phys. Rev. A **73**, 033823 (2006).
[20] J. Perina Jr., Phys. Rev. A **77**, 013803 (2008).
[21] Y. J. Ding, S. J. Lee, and J. B. Khurgin, Phys. Rev. Lett. **75**, 429 (1995).
[22] A. De Rossi and V. Berger, Phys. Rev. Lett. **88**, 043901 (2002).
[23] M. C. Booth, M. Atature, G. Di Giuseppe, B. E. A. Saleh, A. V. Sergienko, and M. C. Teich, Phys. Rev. A **66**, 023815 (2002).
[24] Z. D. Walton, M. C. Booth, A. V. Sergienko, B. E. A. Saleh, and M. C. Teich, Phys. Rev. A **67**, 053810 (2003).
[25] Z. D. Walton, A. V. Sergienko, B. E. A. Saleh, and M. C. Teich, Phys. Rev. A **70**, 052317 (2004).
[26] J. Perina Jr., A. Luks, O. Haderka, and M. Scalora, Phys. Rev. Lett. **103**, 063902 (2009).
[27] J. Perina Jr., A. Luks, and O. Haderka, Phys. Rev. A **80**, 043837 (2009).
[28] B. E. A. Saleh, A. Joobeur, and M. C. Teich, Phys. Rev. A **57**, 3991 (1998).
[29] J. C. Howell, R. S. Bennink, S. J. Bentley, and R. W. Boyd, Phys. Rev. Lett. **92**, 210403 (2004).
[30] M. D'Angelo, Y.-H. Kim, S. P. Kulik, and Y. Shih, Phys. Rev. Lett. **92**, 233601 (2004).
[31] E. Brambilla, A. Gatti, M. Bache, and L. A. Lugiato, Phys. Rev. A **69**, 023802 (2004).
[32] B. M. Jost, A. V. Sergienko, A. F. Abouraddy, B. E. A. Saleh, and M. C. Teich, Opt. Express **3**, 81 (1998).
[33] O. Haderka, J. Perina Jr., and M. Hamar, J. Opt. B: Quantum Semiclass. Opt. **7**, S572 (2005).
[34] O. Haderka, J. Perina Jr., M. Hamar, and J. Perina, Phys. Rev. A **71**, 033815 (2005).
[35] Y. Jiang, O. Jedrkiewicz, S. Minardi, P. Di Trapani, A. Mosset, E. Lantz, and F. Devaux, Eur. Phys. J. D **22**, 521 (2003).
[36] O. Jedrkiewicz, Y.-K. Jiang, E. Brambilla, A. Gatti, M. Bache, L. A. Lugiato, and P. Di Trapani, Phys. Rev. Lett. **93**, 243601 (2004).
[37] O. Jedrkiewicz, E. Brambilla, M. Bache, A. Gatti, L. A. Lugiato, and P. di Trapani, J. Mod. Opt. **53**, 575 (2006).
[38] B. E. A. Saleh and M. C. Teich, *Fundamentals of Photonics* (Wiley, New York, 1991).
[39] Z. Y. Ou, L. J. Wang, and L. Mandel, Phys. Rev. A **40**, 1428 (1989).
[40] L. Mandel and E. Wolf, *Optical Coherence and Quantum Optics* (Cambridge University Press, Cambridge, UK, 1995), Chap. 22.4.7.
[41] M. H. Rubin, Phys. Rev. A **54**, 5349 (1996).
[42] J. P. Torres, F. Macia, S. Carrasco, and L. Torner, Opt. Lett. **30**, 314 (2005).
[43] J. P. Torres, M. W. Mitchell, and M. Hendrych, Phys. Rev. A **71**, 022320 (2005).